Local aspects of the adsorbate-substrate chemical bond in N/Cu(100) and O/Cu(100)

T. Wiell

Department of Physics, Box 530, Uppsala University, S-751 21 Uppsala, Sweden

J. E. Klepeis

Lawrence Livermore National Laboratory, University of California, Livermore, California 94551

P. Bennich, O. Björneholm, N. Wassdahl, and A. Nilsson

Department of Physics, Box 530, Uppsala University, S-751 21 Uppsala, Sweden

Both the occupied and unoccupied adsorbate valence states have been probed by x-ray emission and x-ray absorption spectroscopies for N/Cu(100) and the low coverage phase of O/Cu(100). By carrying out experiments using two different measurement geometries, the adsorbate out-of-plane states ($2p_z$) have been separated from the in-plane states ($2p_{xy}$). The experimental results are compared to the partial density of states (DOS) obtained from full-potential linear muffin-tin orbital calculations, with good agreement in the case of N/Cu(100). This agreement confirms that it is possible to interpret the experimental data in terms of the adsorbate partial DOS. Our combined experimental and theoretical study also provides a detailed understanding of the local chemical bond for N and O adsorbed on Cu(100). [S0163-1829(98)05124-8]

I. INTRODUCTION

Over the years atomic adsorbates on Ni and Cu surfaces have served as prototype systems for strong chemisorption. One of the important aspects to understand in these systems is the nature of the chemical bond between the adsorbate and the surface. The most established experimental technique for electronic structure determination is valence band photoemission spectroscopy (PES). This technique has in particular been very powerful in studying the band structure of overlayer systems. However, there are cases when it is difficult to identify the adsorbate states due to strong overlapping substrate states such as in transition and noble metals. Until recently it has therefore not been straightforward to experimentally study in detail the interaction between the adsorbate and the substrate in the energy region of the substrate d band. We have shown earlier that soft x-ray emission spectroscopy (XES) can be applied to adsorbates.[1–8] An advantage of this technique is that it can be used as a probe of the local density of states (DOS), making it ideally suited for measurements in systems where there is intermixing between the valence states of the different atomic species. XES and PES are complementary since photoemission can measure band dispersion but not the separate contributions from individual atoms, whereas in XES the atom-specific bands, integrated over the whole Brillouin zone, are probed.

In this work we have investigated the electronic structure of two atomic adsorbate systems, N/Cu(100) and the low coverage phase of O/Cu(100). We have chosen to study adsorbates on the Cu(100) surface because the Cu $3d$ band is completely occupied and therefore we expect a significant fraction of the adsorbate $2p$-Cu $3d$ states to be occupied. We have used XES to obtain information about the occupied adsorbate DOS and another well established technique, x-ray absorption spectroscopy (XAS), to obtain information about the unoccupied states. As a first approximation both of these

techniques can be viewed as probes related to the partial DOS. This conclusion is based on the initial and final state rules,[9–13] which say that the intensity of a process is set by the initial state, and the energy distribution by the final state. In XES the final state of the process is only perturbed from the ground state by the presence of a valence hole. For XAS we expect the intensity to be a property of the ground state only since the final state is a core excited state.

These same adsorbate systems have been studied previously by XES, but using white light excitation at normal emission which only probes the in-plane states.[1–3] In this study the samples have been excited using monochromatic synchrotron light tuned to an energy just a few eV above the XAS threshold. In so doing we reduce the possibility of initial state satellites that might distort the measured spectra. We have also measured the XE spectra at both grazing and normal emission angles and have therefore been able to separate out-of-plane from in-plane states. In XAS the in-plane and out-of-plane states were separated by exciting the samples using monochromatic light with the electric field vector oriented either parallel or perpendicular to the surface plane.

In order to obtain a deeper understanding of the experimental results and to confirm the interpretation of the data in terms of the adsorbate partial DOS, we have carried out full-potential linear muffin-tin orbital (FP-LMTO) calculations. The FP-LMTO method[14,15] employs a localized basis that provides a convenient framework for projecting out the individual partial DOS which can then be compared directly to the experimental spectra.

The structural properties of atomic N and O on Cu(100) have been thoroughly studied by various methods including low-energy electron diffraction (LEED), surface extended x-ray absorption fine structure (SEXAFS), electron energy loss spectroscopy (EELS), and scanning tunneling microscopy (STM), to name just a few examples. N/Cu(100) exhibits

only a single phase with a $c(2\times2)$ LEED pattern.[16–22] A detailed SEXAFS study by Lederer *et al.*[21] showed that the N atoms are located in fourfold hollow (FFH) sites at a vertical height of 0.4 Å above the topmost Cu layer which is relaxed outward by 4% relative to bulk Cu. The bond length between the N and its nearest neighbor was determined to be 1.85 Å, and 2.29 Å to the next-nearest neighbor.

Two different phases have been observed for O/Cu(100): a disordered phase[23–26] at low coverages, and at higher coverages a reconstructed $(2\sqrt{2}\times\sqrt{2})R45°$ phase[23–25,27–33] with every fourth Cu row missing in the first layer. For the low coverage phase, SEXAFS measurements by Lederer *et al.*[34] have suggested three different local geometries, all with the O located at or near the FFH site. The simplest FFH geometry is an unreconstructed surface with the O located 0.5 Å above the topmost Cu layer with a bond length of 1.88 Å to the nearest Cu neighbor. The other two geometries, denoted quasi-FFH, involve a displacement of the O away from the FFH site and small displacements of the surrounding Cu atoms with the O located 0.8 Å above the surface. In this work we study the low coverage precursor phase of O/Cu(100) because this structure is similar to that of N/Cu(100).

The electronic structure of N and O adsorbed on Cu(100) has been studied using ultraviolet photoemission spectroscopy (UPS),[35–38] and XES,[1–3] in addition to a number of theoretical treatments.[39–45] Most of the work has focused on O. The primary adsorbate induced states are derived from the interaction between O $2p$ and Cu $3d$ which produces bonding states below the Cu d band and antibonding states above. For O adsorbed on Cu(100) UPS studies show that these states appear at 6 and 1.5 eV below the Fermi level, respectively.[35,37] In the case of N on Cu(100) the corresponding states are located at 5.6 and 1.2 eV below the Fermi level.[35] Using angle resolved UPS, Ling *et al.*[36] assigned the O/Cu(100) bonding state near 6 eV to a O $2p_{xy}$-derived band dispersing between 5.5 and 6.8 eV (xy is parallel to the surface) but found no evidence of O $2p_z$-derived features in this energy range. In addition, they observed an O $2p$ feature at 1.6 eV which was found to contain a mixture of all three O $2p$ components.

II. INSTRUMENTATION

The experiments were performed at the IBM beamline 10-1 at the Stanford Synchrotron Radiation Laboratory (SSRL) using a multipole wiggler with a spherical grating monochromator and a refocusing mirror. The mirror was coated with Ni to reduce the amount of higher order radiation coming through the monochromator. The experiments were performed in a stainless steel UHV chamber, which was pumped by both a turbomolecular and an ion pump down to a base pressure in the mid 10^{-10} Torr region. The chamber was equipped with an XAS detector, an x-ray emission spectrometer, LEED optics, an Auger spectrometer, and an ion gun. The sample was heated using electron bombardment from a filament situated 2 mm behind the sample, which was set to a bias of $+200$ V. The sample was mounted on a cryostat and could be cooled down to liquid nitrogen temperatures; chromel-alumel thermocouples were spot-welded to the side of the crystal for temperature measurements.

The emission spectra were recorded using a multigrating grazing incidence spectrometer with a movable-multichannel-plate-based detector, described in detail elsewhere.[46] The spectra were recorded in second order of diffraction using a 5 m radius spherical grating with 400 lines/mm. An entrance slit in the emission spectrometer was chosen in order to give a resolution of 0.5 eV. The emission spectra were recorded 90° from the incident beam in the plane of the electric field vector. The sample could be rotated around the axis of the incoming beam in order to measure both the normal and grazing emission from the surface. In these experiments the incidence angle was set to 2–5° grazing in order to obtain the highest degree of surface sensitivity. If not otherwise stated, the excitation energy was set to the first resonance as judged by XAS, and the monochromator resolution was set to 4 eV. In addition, an XE spectrum of the substrate L_2 and L_3 transition lines was measured for internal calibration between different runs. These lines were measured in third order of diffraction on the x-ray spectrometer and could thus be detected with the same spectrometer settings as the adsorbate spectra. The uncertainty in the energy scales is estimated to be ±0.3 eV due to the uncertainty in the literature values for the emission energies of the calibration lines.

The absorption spectra were recorded using a partial electron yield detector, with a retardation voltage of 350 and 500 V for N and O, respectively. The absorption spectra were all normalized to the incidence flux as measured by the total photocurrent (I_0) from a gold grid located after the refocusing mirror. Furthermore, in order to remove any possible Cu features in the measured photon energy region, a spectrum from the clean metal surface was taken and used for normalization of the adsorbate spectra. The monochromator was operated at a resolution of 0.2. The grazing spectra were recorded at a 5° incidence angle.

The Cu(100) crystal was cleaned by cycles of Ar ion bombardment at 4×10^{-6} Torr and 500 V for 2 min and subsequently annealed to 600 °C. We checked the surface cleanliness using XES and XAS, and the surface order with LEED.

There are two methods to prepare a N/Cu(100) overlayer. Either by thermal dissociation of ammonia[47] or by low-energy ion bombardment in a N_2 atmosphere.[3,17,19,35,48,49] The latter method was used in this work. Keeping the ambient N_2 pressure at 1×10^{-7} Torr, the ion gun was operated at 500 V for 30 min with the sample at room temperature. The sample was then annealed at 300 °C for 4 min. The overlayer was checked by LEED, where a sharp $c(2\times2)$ pattern was observed.

The O/Cu(100) overlayer was prepared by exposing the clean Cu(100) crystal to O_2 gas at 200 °C. To prepare the low coverage phase, the exposure time was 50 s in an O pressure of 2×10^{-7} Torr (10 L; 1 L=1×10^{-6} Torr s). To insure that the low coverage phase was not contaminated with any of the reconstructed phase, x-ray absorption spectra where recorded at many different coverages (1–8000 L) at normal incidence. The spectra changed drastically when the reconstruction occurred, convincing us that the low coverage measurements where made from an unmixed state.

III. THEORETICAL METHOD

The FP-LMTO method[14,15] we use makes no shape approximation for the crystal potential. The crystal is divided up into regions inside atomic spheres, where Schrödinger's equation is solved numerically, and an interstitial region. As in all LMTO methods the wave functions in the interstitial are Hankel functions. The interpolation procedure we use for evaluating interstitial integrals involving products of Hankel functions is accurate for close-packed but still nonoverlapping atomic spheres.

The basis is composed of one set of s, p, d, and f LMTO's per atom with Hankel function kinetic energy $-\kappa^2 = -0.7$ Ry plus two additional sets of s, p, and d LMTO's per atom with Hankel function kinetic energies of $-\kappa^2 = -1.0$ and -2.3 Ry, for a total of 34 orbitals per atom. The Hankel functions decay exponentially as $e^{-\kappa r}$; we find that taking energies $-\kappa^2$ closer to zero leads to an inaccurate description of the exponential decay of the charge density just outside the surface. We also find that a layer of empty spheres is needed outside the surface in order that the interpolation procedure be sufficiently accurate in this region. The charge density beyond this layer of empty spheres is small enough that only a single layer is needed. However, these empty spheres do not contribute to the basis but merely improve the accuracy of the interpolation procedure. The angular momentum sums involved in the interpolation procedure are carried up to $\ell = 6$ for all of the spheres. The accuracy of our FP-LMTO method for surface calculations has been demonstrated previously.[50,51]

The calculations presented here are based on the local density approximation (LDA), using the exchange-correlation potential of Ceperley and Alder,[52] as parametrized by Vosko, Wilk, and Nusair.[53] The scalar-relativistic Schrödinger equation was solved self-consistently for the clean, N-covered and O-covered Cu(100) surfaces. The Cu $4s$, $4p$, $3d$, and $4f$, states and the adsorbate $2s$, $2p$, $3d$, and $4f$ states were all treated as valence. The semicore Cu $3p$ states were treated as full band states by carrying out a "two-panel" calculation. The second panel band calculation for the semicore states included the Cu $4s$, $3p$, and $3d$ states as well as the adsorbate $2s$, $2p$, and $3d$ states. The Brillouin zone sums were carried out using the tetrahedron method.[54] In the case of the FFH geometries we used 36 irreducible **k** points ($16 \times 16 \times 2$ shifted mesh) in the first panel and three irreducible **k** points ($4 \times 4 \times 2$ shifted mesh) in the second panel. The quasi-FFH geometry for O has lower symmetry and thus the number of irreducible **k** points were larger, 64 and four for the respective panels. The Cu sphere radii were chosen to be 2% smaller than half the bulk Cu bond length while the adsorbate sphere radii were chosen to be 2% smaller than the difference between the adsorbate nearest-neighbor bond length and the Cu sphere radius.

All of the calculations were carried out using the experimental bulk Cu lattice constant. The multilayer atomic relaxation of the clean Cu(100) surface has been calculated recently using the same FP-LMTO method[55] and we use this geometry for the clean surface calculations presented here. For the N/Cu(100) system we have used the local $c(2 \times 2)$ geometry obtained from the SEXAFS study of Lederer et al.[21] In the case of the low coverage phase of O/Cu(100)

we have considered both the FFH geometry and one of the displaced geometries (denoted quasi-FFH I) postulated by Lederer et al.[34] However, we have artificially used a $c(2 \times 2)$ surface unit cell in order to make the calculations tractable. This approximation introduces extra O-O interactions but since we find them to be small the approximation should be minor. Each of the (100) surfaces were approximated by supercells consisting of either 7 or 15 Cu(100) layers plus the equivalent of 11 vacuum "layers." All of the partial DOS calculations presented here were carried out using 15 Cu(100) layers except for those corresponding to the O/Cu(100) FFH geometry where 7 layers were used. Seven layers were also used in the calculations for the Mulliken overlap populations.

The partial DOS and overlap populations have been calculated using a Mulliken decomposition[56] as described in detail by Hoffmann.[57] In particular, the overlap populations are positive for bonding states and negative for antibonding. The integral over all of the occupied states scales similar to, but not identical to, a bond order. A Mulliken decomposition is inherently nonunique and this ambiguity is further compounded by the fact that we choose to project out against a particular set of orbitals, the numerical basis functions obtained from the self-consistent calculations. This projection clearly depends on the characteristics of these orbitals but the results are nonetheless useful because the most important characteristics are that the orbitals are well localized and they possess the appropriate symmetry properties. One further complication arises due to our use of a triple-κ basis which makes the interpretation of the DOS well above the Fermi level problematic. However, the interpretation near and below the Fermi level generally does not suffer from the
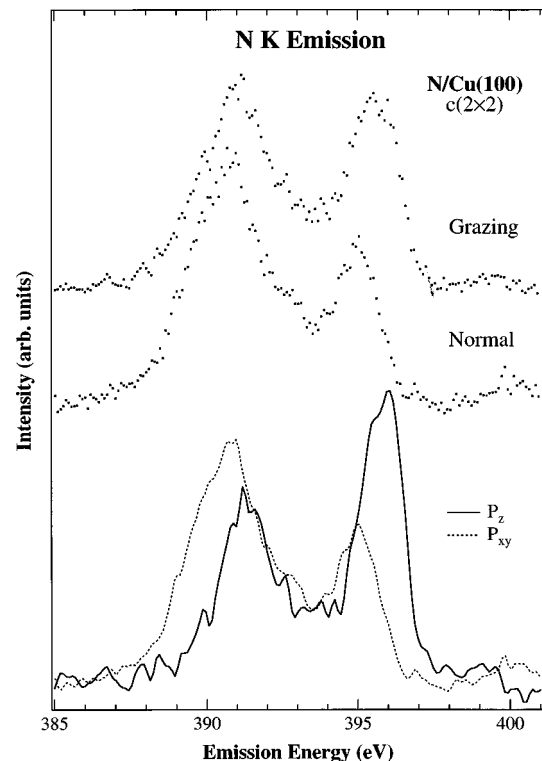

FIG. 1. Nitrogen K emission from N/Cu(100) at grazing and normal emission angles. The $2p_{xy}$ and extracted $2p_z$ spectra are also shown.
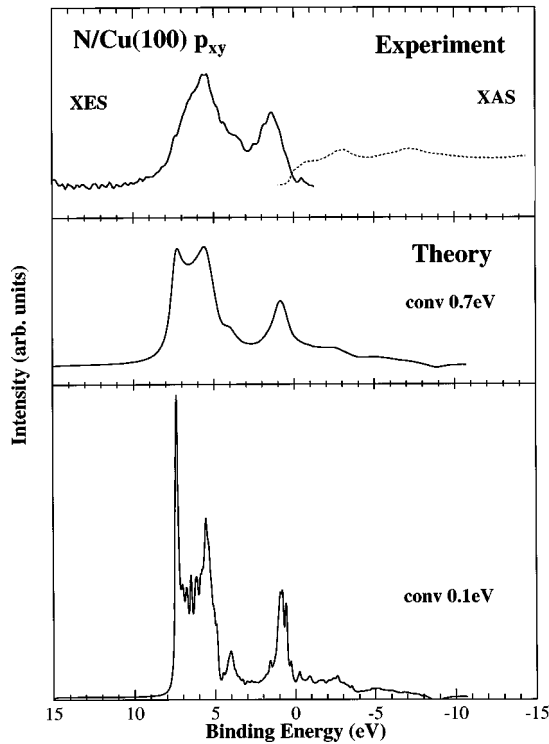
FIG. 2. The experimental N $2p_{xy}$ spectra are compared with the calculated partial DOS for N/Cu(100). The left part of the top spectra shows the x-ray emission spectrum while the right part shows the x-ray absorption. The middle and bottom plots show the calculated N $2p_{xy}$ DOS convoluted with 0.7 and 0.1 eV FWHM Lorentzians, respectively.

same difficulty. The Brillouin zone sums for the DOS were performed with the tetrahedron method[54] using 45 irreducible **k** points ($16 \times 16 \times 1$ unshifted mesh) for the FFH geometries and 81 **k** points for the O/Cu(100) quasi-FFH geometry.

IV. RESULTS

To start with we would like to demonstrate how we can separate the different $2p$ components using N/Cu(100) spectra as an example. Figure 1 shows the x-ray emission data both at grazing and normal emission angles, as well as $2p_{xy}$ and the extracted $2p_z$ (see below) for atomic N on Cu(100). It is assumed that half of the intensity at grazing emission comes from $2p_{xy}$ and the other half from $2p_z$. With this assumption $2p_z$ is calculated by subtracting 50% of the normal spectra from the grazing spectra, both normalized to the same area. Both $2p_{xy}$ and $2p_z$ have been smoothed to make it easier to see the shape of the spectra. The small structure seen at 400 eV arises from the elastic scattering of the exciting photon.

In order to compare the spectra for the two adsorbate systems, the energy axes can be rescaled into binding energy relative to the Fermi level. This can be done by subtracting the XPS binding energy of the adsorbate $1s$ core level since the Fermi level in the emission spectra will be located at that energy (which is also the maximum emission energy possible from a 1s core hole). Note that the binding energy scale should be inverted compared to the emission energy scale
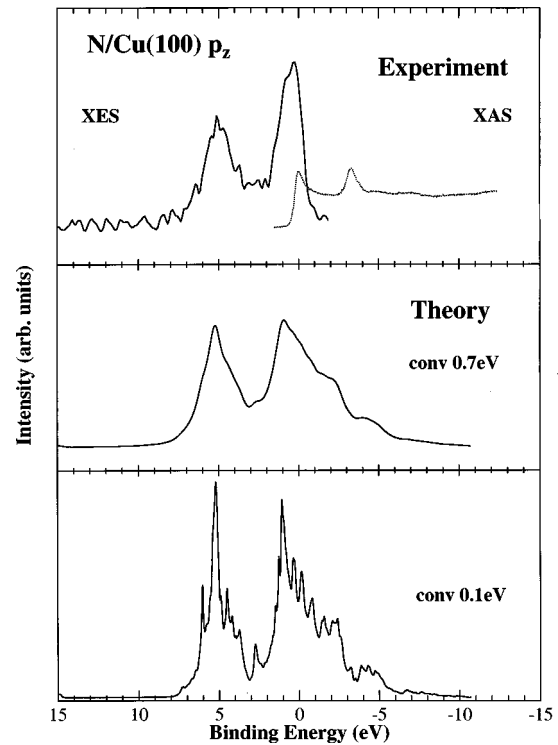

FIG. 3. A comparison between the experimental and calculated N $2p_z$ DOS for N/Cu(100).

(i.e., low emission energy corresponds to high binding energy, and vice versa). N/Cu(100) has an XPS binding energy of 396.3 eV,[3] which is located above the high-energy peak for $2p_{xy}$, indicating that this state is completely occupied. The low coverage phase of O/Cu(100) has an XPS binding energy of 529.5 eV.[58]

In Figs. 2–5 we compare the experimental adsorbate $2p$ data with the calculated FP-LMTO partial DOS. The O/Cu(100) calculation is for the O atom located in the quasi-FFH site 0.8 Å above the first Cu layer.[34] The bottom two plots in each figure show the calculated DOS convoluted with 0.7 and 0.1 eV full width at half maximum (FWHM) Lorentzians. The 0.7 eV FWHM Lorentzian was chosen in order to obtain a theoretical plot comparable to the experimental spectra where there is broadening due to the width of the core hole as well as the finite instrument resolution of 0.5 eV. Before discussing the comparison we note that the calculations do not treat the full quasiparticle problem and therefore the calculated bandwidths may differ from the experimental ones. Furthermore, the x-ray emission process involves a core hole in the initial state which could alter the relative intensities for the different states. The figures also show the XA spectra measured in normal and grazing incidence. Since the final state in the XA process contains a core hole there could be significant differences compared with the calculated empty DOS.[13]

Despite the potential sources of discrepancy just mentioned, we see that in the case of N (Figs. 2 and 3) there is very good agreement between the calculated partial DOS and the experimental XES data. For N $2p_{xy}$ (Fig. 2) the low-energy XES peak at a binding energy of 6 eV with a shoulder on the low-energy side coincides with the double peak structure in the calculation. At a binding energy of 4 eV we
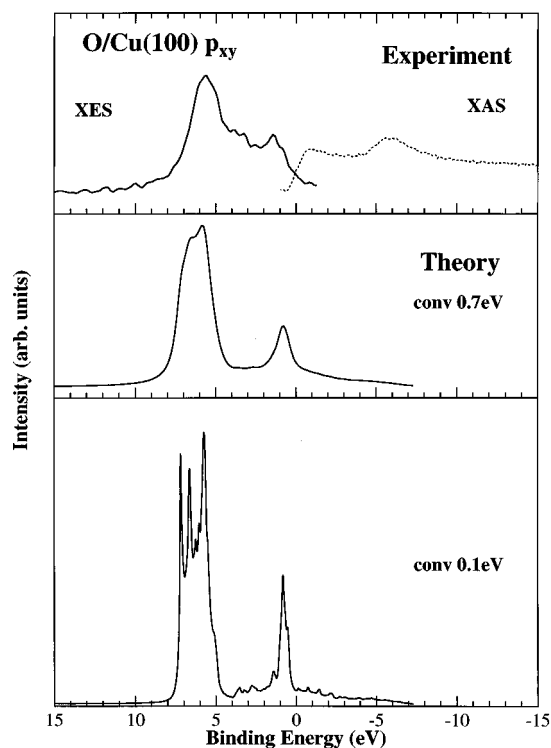
FIG. 4. The experimental O $2p_{xy}$ spectra for the low coverage phase of O/Cu(100) are compared with the calculated partial DOS. In the calculations the O atom is located in a quasi-FFH site 0.8 Å above the topmost Cu layer.

FIG. 5. Experimental and calculated O $2p_z$ DOS for the low coverage phase of O/Cu(100). The calculations correspond to a quasi-FFH site.

see a feature in both the experimental and calculated DOS. In the bottom plot this feature is very clear, whereas in the experiment it is broadened and overlaps with the main peak. Convoluting the calculated DOS with a 0.7 eV FWHM Lorentzian results in a plot which reproduces the experimental data very well in this energy range. Near the Fermi level, theory and experiment are also in good agreement. We see that the experimental XES peak centered at a binding energy of 1–1.5 eV has dropped nearly to zero at the Fermi level. With regard to the unoccupied states (the XAS spectrum in the top plot), we see similar features in both the experiment and the calculations, although there is some discrepancy in the energy positions. The peak at 2.5 eV in the XAS spectrum corresponds to a similar feature in the calculations at the same energy, whereas the broad XAS structure at 7 eV is identified with the broad calculated feature at 4–8.5 eV.

In Fig. 3 the agreement between theory and experiment for N $2p_z$ is also very good for the occupied states. Both the main peak at a binding energy of 5 eV as well as the strong peak near the Fermi level are reproduced in the calculations. The fact that the peak near the Fermi level in the lower two plots is only partially occupied is also in good agreement with the experiment. However, there are some differences between the calculations and the unoccupied XAS spectrum. In the absorption spectrum there are two strong peaks, one at the Fermi level and the other 3 eV above. In the calculations the second peak appears to be closer to the Fermi level in the form of a shoulder on the high-energy side of the peak centered at the Fermi level. This could be caused by the core hole final state in XAS. We also see two weak structures at 4.5 and 7 eV in both the XA spectrum and the calculations.
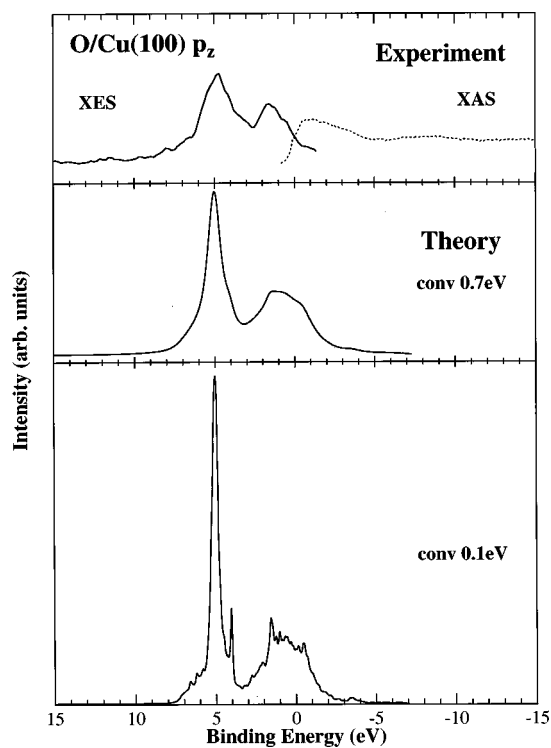
In the case of the O $2p_{xy}$ DOS for the low coverage phase of O/Cu(100) (Fig. 4) the agreement between theory and experiment is not as good as that for N/Cu(100). In the calculated DOS of Fig. 4 the main peak is at the same energy as in the experiment. Near the Fermi level a sharp peak is seen in the calculated DOS whereas the corresponding peak in the experimental spectrum is broader and at higher binding energy. The most important difference between the calculated DOS and the experimental data is the absence of any significant states at 2–4 eV in the calculated DOS. In particular, a feature at a binding energy of 4 eV is clearly seen in the experimental data for both O/Cu(100) and N/Cu(100) and is also present in the N/Cu(100) calculation (Fig. 2), but is missing from the O/Cu(100) calculation. With regard to the unoccupied states, the intensity seen just above the Fermi level in the absorption spectrum is reproduced in the calculations whereas the peak at 6 eV is not seen.

The calculated O $2p_z$ DOS shown in Fig. 5 are in better agreement with the experimental data than the O $2p_{xy}$ DOS. Both peaks seen in x-ray emission appear in the calculations, although the calculated peak at high binding energy is narrower. In addition, the presence of a finite DOS above the Fermi level is also seen in both XES and XAS. Furthermore, the peak at 1 eV in the XA spectrum also appears in the calculated DOS.

In order to investigate whether the absence of a peak at a binding energy of 4 eV in the calculated O $2p_{xy}$ DOS in Fig. 4 is caused by our choice of the quasi-FFH geometry, we have also carried out calculations for a pure FFH geometry. In the SEXAFS study of Lederer et al.[34] three different local geometries were proposed with the best fit to the SEXAFS data occurring for two geometries denoted quasi-FFH I and
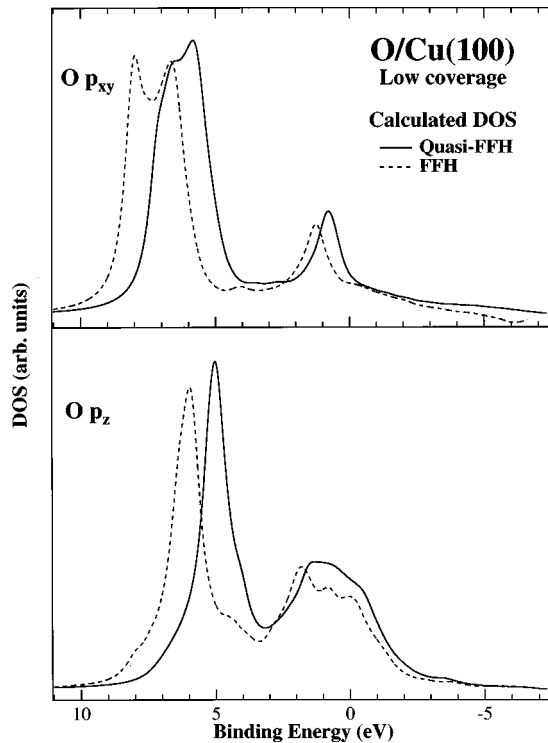
FIG. 6. A comparison of the calculated DOS for two different adsorption geometries for the low coverage phase of O/Cu(100). The top plot shows the O $2p_{xy}$ DOS and the lower plot shows O $2p_z$. The solid lines correspond to the quasi-FFH geometry and the dotted lines to the pure FFH geometry.

II (the data could not distinguish between them). In these two geometries the O atom is located 0.8 Å above the topmost Cu layer and is displaced from the pure FFH site. The calculations presented in Figs. 4 and 5 correspond to the quasi-FFH I geometry. In Fig. 6 we compare these quasi-FFH calculations with those corresponding to a pure FFH geometry, also proposed by Lederer *et al.*,[34] where the O atom is located 0.5 Å above the first Cu layer. We choose this geometry because the O is closer to the Cu surface than for the other two geometries and thus it more closely resembles the N/Cu(100) geometry. We note that in contrast to the SEX-AFS study, we find that the total energy for the pure FFH geometry is 0.21 eV per O atom lower in energy than the quasi-FFH I geometry.

The top part of Fig. 6 shows the calculated O $2p_{xy}$ DOS for the two geometries while the bottom shows the corresponding O $2p_z$ DOS. All of the DOS have been convoluted with 0.7 eV FWHM Lorentzians. The solid lines correspond to the quasi-FFH geometry and the dotted lines to the pure FFH geometry. We can see that all of the states shift to higher binding energy for the FFH structure. This result is due to the fact that the O atom is closer to the surface in the FFH geometry which reduces the O-Cu surface dipole, thereby lowering the electrostatic potential of the O relative to the bulk Cu Fermi level. We note that the low-energy double peaked structure in the FFH $2p_{xy}$ DOS is more differentiated. In general the agreement between theory and experiment is not improved and in fact the shift to higher binding energies worsens the agreement for the FFH calculations. It is therefore likely that neither geometry is correct by itself. One possible interpretation is that the low coverage phase of
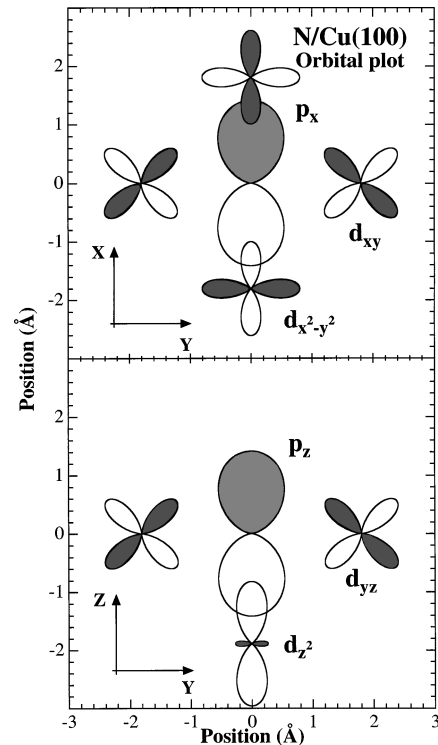

FIG. 7. A plot of the spherical harmonics for N $2p$ and Cu $3d$ states. They have been calculated for a radius that encloses 99% of the radial wave function and then uniformly scaled up to more clearly show the orbital overlaps. The top figure shows the surface from above with one N atom sitting in an FFH site surrounded by four Cu atoms. The bottom picture shows a side view with a Cu atom from the second layer located directly below the N.

O/Cu(100) consists of multiple local O geometries. The experimental spectra would then represent an average over all of these geometries. Such averaging could account for the intensity at 2–4 eV in the O $2p_{xy}$ XES spectrum as well as the larger width (compared to the calculated DOS) of the lower energy O $2p_z$ peak. We also note that the 1 eV shift of the main peak in the O $2p_z$ spectrum is similar to the shift observed when going from the low coverage phase of O/Cu(100) to the strongly reconstructed $(2\sqrt{2} \times \sqrt{2})$R45° phase where the O atoms are located only 0.1 Å above the first Cu layer.[59]

V. DISCUSSION

We have shown that the FP-LMTO calculations for N/Cu(100) very closely reproduce the experimental data and therefore we will use these calculations to extract information about the nature of the N-Cu bond. In order to facilitate the discussion of the adsorbate-induced states we will first characterize the different types of valence orbital interactions.

In Fig. 7 we plot the spherical harmonics for atomic N $2p$ orbitals surrounded by atomic Cu $3d$ orbitals in an ideal, FFH adsorbate geometry where the N atom is located at the same vertical height as the first-layer Cu atoms. The upper part of the figure shows the in-plane (xy) atomic orbitals while the lower part shows the out-of-plane (yz) orbitals. We have chosen to plot only the N $2p_x$ and $2p_z$ orbitals as
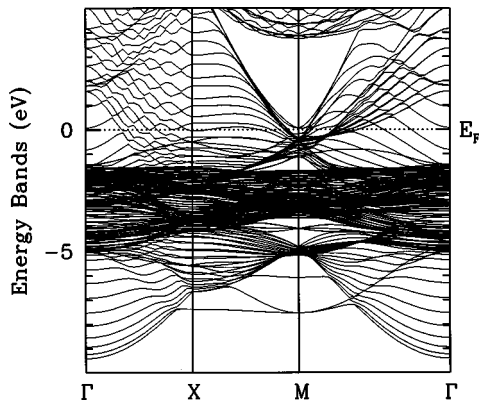
FIG. 8. The first principles energy bands calculated for the $c(2 \times 2)$ N/Cu(100) surface

well as selected Cu $3d$ orbitals which have nonzero overlap with the N $2p$ orbitals. The adsorbate geometry has C_{4v} symmetry and therefore the N $2p_y$ and Cu $3d_{xz}$ orbitals are obtained by a 90° rotation about the z axis. The N $2p_x$ orbital forms both σ and π bonds with the substrate. The σ bonds result from the overlap with the first-layer Cu $3d_{x^2-y^2}$, $3d_{z^2}$, and $4s$ orbitals, while the π bonds arise from the overlap with the Cu $3d_{xy}$ orbitals in the first layer and the $3d_{xz}$ orbital on the second-layer Cu atom located directly below the adsorbate. For this ideal geometry the remaining nearest-neighbor Cu orbitals have zero overlap with the N $2p_x$ orbital. The lower portion of Fig. 7 shows that the N $2p_z$ orbital forms π bonds with the first-layer Cu $3d_{yz}$ and $3d_{xz}$ orbitals. The N $2p_z$ σ bonds result from the overlap with the second-layer Cu $3d_{z^2}$ and $4s$ orbitals.

The actual adsorbate geometry involves a displacement of the N atom outwards away from the first Cu layer by 0.4 Å. This displacement makes possible contributions from additional Cu orbitals other than those shown for the ideal geometry in Fig. 7, and also introduces some mixing of the N $2p_{xy}$ and $2p_z$ orbitals in the σ and π bonds described above. However, as we will see below, the primary contributions to the adsorbate-induced states are similar to those of the simpler ideal geometry.

We plot the calculated energy bands for the $c(2 \times 2)$ N/Cu(100) surface in Fig. 8. We can identify some surface states and resonances. For example, there is a flat N-derived surface band 7.5 eV below the Fermi level along $X \rightarrow M$ in Fig. 8. A number of surface resonances are also visible, such as the continuation of the 7.5 eV surface band near the X point which disperses upwards to 5 eV at the Γ point in Fig. 8. The region with the highest density of bands corresponds to the Cu $3d$ states. Adsorbate-induced bands are clearly visible around the M point of the SBZ, in part because there are gaps in the projected bulk bands around this point. However, it is more difficult to distinguish the surface-derived bands when they overlap with the large density of Cu states.

There are six predominantly surface-derived bands arising from the bonding and antibonding combinations of the N $2p_x$, $2p_y$, and $2p_z$ orbitals with the underlying Cu $3d$ and $4s$ orbitals. Each of these six bands contains both σ and π contributions at different points in the SBZ. A straightforward tight-binding analysis of the model problem indicates that the N-derived surface states will be bonding or antibond-
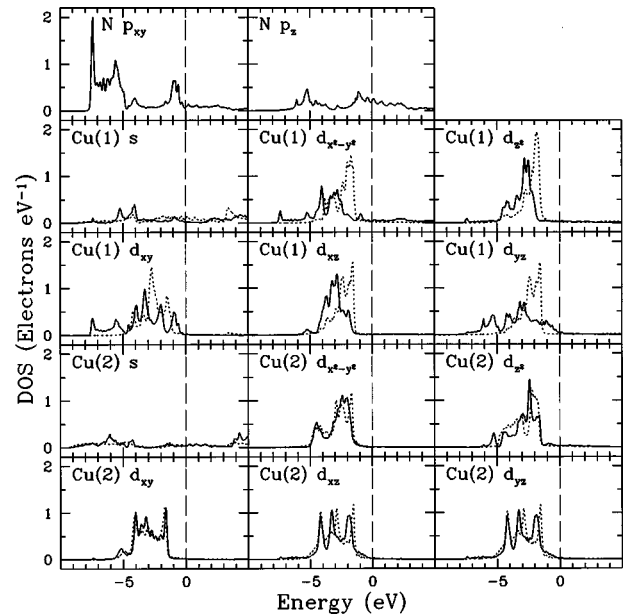

FIG. 9. The calculated N $2p$, Cu $4s$, and Cu $3d$ partial DOS for both clean Cu(100) and N/Cu(100). For each of the Cu orbitals the solid line represents N/Cu(100) and the dotted line clean Cu(100). The label Cu(1) refers to the closest Cu neighbor displaced along the y axis from the adsorbed N while Cu(2) refers to the second-layer atom located directly below the N atom along the z axis. All of the DOS have been convoluted with a 0.1 eV FWHM Lorentzian and are plotted on the same vertical scale.

ing at the M point and nonbonding at the Γ point, for both σ and π interactions. We therefore expect that the bonding bands will disperse downwards from the zone center to the edges and the antibonding bands upwards. At the X point the interactions are generally a mixture of nonbonding as well as bonding and antibonding. The σ interactions between N $2p_x$ and the first layer Cu $3d_{x^2-y^2}$, $3d_{z^2}$, and $4s$ are bonding or antibonding while the π interaction with the first layer Cu $3d_{xy}$ is nonbonding. The reverse is true for N $2p_y$ with the σ interactions being nonbonding and the π interactions bonding or antibonding. The π interaction of N $2p_z$ where the first layer Cu $3d_{yz}$ is bonding or antibonding while the π interaction with $3d_{xz}$ is nonbonding. In all cases the interactions of the N orbitals with those on the second layer Cu are independent of $\mathbf{k}$.

In order to identify the N-derived bands in both the experimental spectra and the calculated density of N $2p$ states we study how the calculated Cu DOS are modified by the adsorption of N. Furthermore, from an analysis of Mulliken overlap populations (MOP's) we can deduce the bonding character of the bands; the MOP's are positive for bonding states and negative for antibonding states. In Fig. 9 the calculated N and Cu partial DOS for both clean Cu(100) and N/Cu(100) are shown. For each of the Cu orbitals the solid line represents N/Cu(100) and the dotted line clean Cu(100). The corresponding MOP's between N $2p$ and different Cu orbitals are plotted in Fig. 10 where the solid lines correspond to N $2p_{xy}$ and the dotted lines to N $2p_z$. In both figures the label Cu(1) refers to the closest Cu neighbor displaced along the y axis from the adsorbed N (left or right of the N atom in Fig. 7) while Cu(2) refers to the second-layer atom located directly below the N atom along the z axis. In
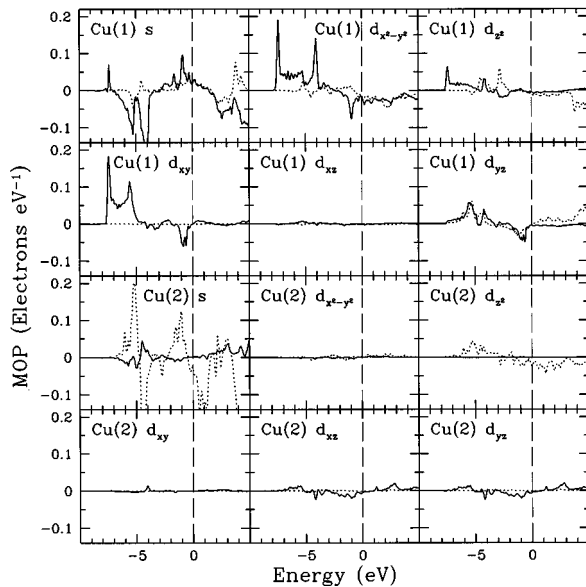
FIG. 10. The calculated Mulliken overlap populations between N $2p$ and different Cu orbitals for N/Cu(100). The solid lines correspond to N $2p_{xy}$ and the dotted lines to N $2p_z$. The label Cu(1) refers to the closest Cu neighbor displaced along the y axis from the adsorbed N while Cu(2) refers to the second-layer atom located directly below the N atom along the z axis. All of the MOP's have been convoluted with a 0.1 eV FWHM Lorentzian and are plotted on the same vertical scale, except that all of the N $2p_z$ MOP (dotted lines) have been uniformly scaled by a factor of 2 for clarity of presentation.

Fig. 10 the first- and second-layer Cu $4s$, $3d_{x^2-y^2}$, and $3d_{z^2}$ orbitals correspond to σ bonds while the remaining orbitals correspond to π bonds, as defined for the ideal geometry in Fig. 7.

In Fig. 9 we can identify four distinct features in the N $2p_{xy}$ DOS at approximately 7.5, 5.5, 4, and 1 eV below the Fermi level. All four of these features can be tentatively identified with flat surface bands or resonances in Fig. 8, as will be demonstrated below. From the discussion in conjunction with Fig. 7 we expect a strong coupling between N $2p_{xy}$ and Cu(1) $3d_{x^2-y^2}$, $3d_{z^2}$, $3d_{xy}$, and $4s$. The DOS in Fig. 9 for these four Cu orbitals, and in particular Cu(1) $3d_{x^2-y^2}$ and $3d_{xy}$, exhibit significant changes upon N adsorption with distinct new features at the same energies as the features in the N $2p_{xy}$ DOS.

The MOP's in Fig. 10 provide additional information which allows us to make assignments of distinct features in the DOS to elements of the band structure. In particular, the peak in the N $2p_{xy}$ DOS near 7.5 eV is strongly bonding and clearly arises from the lowest surface band along $X \rightarrow M$ in Fig. 8, which is consistent with the strongly bonding σ and π interactions at the M point. Similarly, we surmise that the DOS peak near 5.5 eV corresponds to a surface resonance at the X point. This conclusion is supported by the MOP in Fig. 10 which show essentially nonbonding σ interactions with Cu(1) $3d_{x^2-y^2}$ and $3d_{z^2}$ but a strongly bonding π interaction with Cu(1) $3d_{xy}$. We note that the splitting of the two lower bands at X is approximately related to the differing strengths of the σ and π interactions. At the Γ point the surface resonances are nonbonding and are likely related to the onset

seen in the N $2p_{xy}$ DOS and MOP's around 5 eV. We assign the N $2p_{xy}$ DOS feature at 4 eV primarily to a surface resonance at the X point. This resonance is a continuation of the surface state in the gap around 4 eV at the M point. The MOP support this assignment because they show a bonding σ interaction with Cu(1) $3d_{x^2-y^2}$ and $3d_{z^2}$, an antibonding σ interaction with Cu(1) $4s$, and a nonbonding π interaction with Cu(1) $3d_{xy}$. This feature has a large contribution from the Cu orbitals which is consistent with the presence of a surface state for the clean Cu(100) surface in the same M point gap but at a slightly lower energy. From approximately 1–4 eV the DOS are dominated by Cu $3d$ with little contribution from N $2p$, and likely arise from states throughout the whole zone. The MOP are primarily nonbonding in this energy range. The N $2p_{xy}$ DOS near 1 eV have antibonding character and can be assigned to the surface resonance seen in Fig. 8 along $M \rightarrow \Gamma$ just above the bulk Cu d band. Finally, the MOP's show nonzero interactions between N $2p_{xy}$ and Cu(1) $3d_{yz}$. These interactions result from the displacement of the N atom outwards from the ideal symmetric position discussed in connection with Fig. 7. Furthermore, the N $2p_{xy}$ bands will also have some N $2p_z$ orbital character for the same reason.

We expect N $2p_z$ to interact most strongly with Cu(1) $3d_{yz}$, Cu(2) $3d_{z^2}$, and Cu(2) $4s$ which is confirmed by the MOP's in Fig. 10. We also see that, in comparison to N $2p_{xy}$, the bonding-antibonding split is smaller for N $2p_z$, indicating a weaker interaction with the substrate. The interaction is weaker because N $2p_z$ forms predominantly π bonds with the first Cu layer and the σ bonds to the second layer are weaker due to the larger N-Cu bond length.

The dominant features in the N $2p_z$ DOS in Fig. 9 are at approximately 6, 5.5, and 1 eV, with the latter structure showing an extended tail above the Fermi level. There is essentially no contribution to the lowest surface band at 7.5 eV below the Fermi level. We can assign the 6 eV feature to the surface state around the M point which becomes a surface resonance at the other points in the Brillouin zone. The primary feature at 5.5 eV likely corresponds to the surface resonance at the X point, just as in the case of N $2p_{xy}$. Similarly, the feature at 1 eV can be assigned in part to the surface resonance along $M \rightarrow \Gamma$ just above the bulk Cu d band. One important difference relative to N $2p_{xy}$ is that the antibonding states extend above the Fermi level and thus are partially unoccupied. The MOP's in Fig. 10 suggest that these states arise from the σ interaction with the second layer.

Under the circumstance where both the bonding and antibonding states are fully occupied there is a net reduction in the strength of the chemical bond. It is therefore an important point that the calculated DOS and MOP's indicate that there are partially unoccupied antibonding N $2p_z$ but not $2p_{xy}$ states. This is also clearly seen in the experimental spectra in Fig. 1 where the whole N $2p_z$ spectrum is shifted towards lower energies. Therefore the σ interaction of N $2p_z$ with the second layer is important for the chemisorption energetics, despite the fact that it is weaker than some of the N $2p_{xy}$ σ interactions.

Our results confirm the general picture obtained in previous work of bonding states below and antibonding states above the bulk Cu d band. The states with the largest bond-

ing character occur at the M point and have a large N $2p$ contribution while the nonbonding states are predominantly Cu $3d$. However, there are some small differences between theory and experiment. In Figs. 2 and 3 both N $2p_{xy}$ and $2p_z$ appear to have larger adsorbate contributions in the Cu $3d$ region than predicted by the calculations. Furthermore, the first distinct feature at 7.5 eV in the calculated N $2p_{xy}$ DOS appears only as a shoulder on the 5.5 eV peak in the XES spectrum. As discussed above, this feature arises from the very flat band along $X \rightarrow M$ at 7.5 eV in Fig. 8. Conversely, the experiments would seem to indicate that this band has some dispersion rather than being completely flat.

If we apply the general interpretation of the N $2p$ DOS to the results for O we obtain essentially the same picture with bonding states below and antibonding states above the bulk Cu d band and nonbonding states with a large Cu $3d$ contribution in between. From Figs. 4 and 5 we can see that compared to N the nonbonding states appear to have a larger fraction of O $2p$ character. In addition, the N $2p_{xy}$ DOS exhibit a larger contribution to the bonding states than the antibonding states whereas the reverse is true for the N $2p_z$ DOS. In the case of O Figs. 4 and 5 show that both the $2p_{xy}$ and the $2p_z$ have a larger contribution to the bonding states, indicating a more polar bond which is consistent with the lower orbital energy for O $2p$ compared to N $2p$.

VI. SUMMARY

We have probed both the occupied and unoccupied adsorbate valence states with XES and XAS for N/Cu(100) and the low coverage phase of O/Cu(100). By carrying out experiments using two different measurement geometries, the adsorbate $2p_z$ states have been separated from the $2p_{xy}$ states. The favorable comparison between the experimental results and FP-LMTO calculations for N/Cu(100) confirms the validity of interpreting the experimental data in terms of the adsorbate partial DOS. Recent calculations for N on Cu(100) simulating the x-ray emission process support this simple one electron picture.[60] The combination of XES and XAS measurements and FP-LMTO calculations have enabled us to obtain a detailed understanding of the local chemical bond for N and O adsorbed on Cu(100). Bonding states are found below and antibonding states above the bulk Cu d band with nonbonding states in between. This splitting is driven primarily by the local adsorbate $2p$–Cu $3d$ interaction. The bonding and antibonding states contain a large contribution from the adsorbate $2p$ orbitals whereas the nonbonding states are of predominantly Cu $3d$ character. The adsorbate $2p_{xy}$ orbitals couple strongly to the first-layer Cu $3d_{x^2-y^2}$, $3d_{xy}$, and $4s$ orbitals. The adsorbate $2p_z$ orbital couples primarily to the first-layer Cu $3d_{xz}$ and $3d_{yz}$ orbitals and the second-layer Cu $3d_{z^2}$ and $4s$ orbitals. The $2p_z$ orbital interacts more weakly with the substrate leading to a smaller bonding-antibonding splitting in comparison to the splitting for $2p_{xy}$. The primary difference between N and O adsorption is a more polar bond for O which manifests itself as a stronger asymmetry in the contribution of the O orbitals to the bonding versus antibonding states.

[1] N. Wassdahl, A. Nilsson, T. Wiell, H. Tillborg, L.-C. Duda, J. H. Guo, N. Mårtensson J. Nordgren, J. N. Andersen, and R. Nyholm, Phys. Rev. Lett. **69**, 812 (1992).

[2] H. Tillborg, A. Nilsson, T. Wiell, N. Wassdahl, N. Mårtensson, and J. Nordgren, Phys. Rev. B **47**, 16 464 (1993).

[3] T. Wiell, H. Tillborg, A. Nilsson, N. Wassdahl, N. Mårtensson, and J. Nordgren, Surf. Sci. **304**, L451 (1994).

[4] A. Nilsson, P. Bennich, T. Wiell, N. Wassdahl, N. Mårtensson, J. Nordgren, O. Björneholm, and J. Stöhr, Phys. Rev. B **51**, 10 244 (1995).

[5] A. Nilsson, M. Weinelt, T. Wiell, P. Bennich, O. Karis, N. Wassdahl, J. Stöhr, and M. Samant, Phys. Rev. Lett. **78**, 2847 (1997).

[6] A. Nilsson, N. Wassdahl, M. Weinelt, O. Karis, T. Wiell, P. Bennich, J. Hasselström, A. Fölisch, J. Stöhr, and M. Samant, Appl. Phys. A: Mater. Sci. Process. **65**, 147 (1997).

[7] P. Bennich, T. Wiell, O. Karis, M. Weinelt, N. Wassdahl, A. Nilsson, M. Nyberg, L. G. M. Pettersson, J. Stöhr, and M. Samant, Phys. Rev. B **57**, 9274 (1998).

[8] A. Nilsson, J. El. Spec. Rel. Phenom. (to be published).

[9] A. F. Starace, Phys. Rev. B **5**, 1773 (1972): V. I. Grebennikov, Yu. A. Babanov, and O. B. Sokolov, Phys. Status Solidi B **79**, 423 (1977); **80**, 73 (1977).

[10] U. von Barth and G. Grossmann, Phys. Rev. B **25**, 5150 (1982).

[11] C. O. Almbladh and L. Hedin, in *Handbook of Synchronized Radiation*, edited by E. E. Koch (North-Holland, Amsterdam, 1983), Vol. 1b.

[12] J. Stöhr and Y. Wu, in *New Directions in Research with 3rd Generation Soft X-Ray Synchrotron Radiation Sources*, Vol. 254 of NATO *Advanced Study Institute, Series E: Applied Sciences*, edited by A. S. Schlachter and F. J. Wuilleumier (Kluwer Academic, Dordrecht, The Netherlands, 1994), p. 221.

[13] E. O. F. Zdansky, A. Nilsson, H. Tillborg, O. Björneholm, N. Mårtensson, J. N. Andersen, and R. Nyholm, Phys. Rev. B **48**, 2632 (1993); A. Nilsson and N. Mårtensson, Physica B **208/209**, 19 (1995).

[14] M. Methfessel, Phys. Rev. B **38**, 1537 (1988).

[15] M. Methfessel, C. O. Rodriguez, and O. K. Andersen, Phys. Rev. B **40**, 2009 (1989).

[16] R. N. Lee and H. E. Farnswoth, Surf. Sci. **3**, 461 (1965).

[17] J. M. Burkstrand, G. G. Kleiman, G. G. Tibbetts, and J. C. Tracy, J. Vac. Sci. Technol. **13**, 291 (1976).

[18] G. G. Kleiman and J. M. Burkstrand, Solid State Commun. **21**, 5 (1977).

[19] H. C. Zeng, R. N. S. Sodhi, and K. A. R. Mitchell, Surf. Sci. **188**, 599 (1987).

[20] H. C. Zeng, R. A. McFarlane, and K. A. R. Mitchell, Surf. Sci. **208**, L7 (1989).

[21] T. Lederer, D. Arvanitis, M. Tischer, G. Comelli, L. Tröger, and K. Baberschke, Phys. Rev. B **48**, 11 277 (1993).

[22] M. Sotto, S. Gauthier, F. Pourmir, S. Rousset, and J. Klein, Surf. Sci. **371**, 36 (1997).

[23] R. Mayer, C. S. Zheng, and K. G. Lynn, Phys. Rev. B **33**, 8899 (1986).

[24] M. Wuttig, R. Franchy, and H. Ibach, Surf. Sci. **213**, 103 (1989).

[25] M. Wuttig, R. Franchy, and H. Ibach, Surf. Sci. **224**, L979 (1989).

[26] T. Fujita, Y. Okawa, Y. Matsumoto, and K. Tanaka, Phys. Rev. B **54**, 2167 (1996).

[27] L. McDonnell and D. P. Woodruff, Surf. Sci. **46**, 505 (1974).

[28] P. Hofmann, R. Unwin, W. Wyrobisch, and A. M. Bradshaw, Surf. Sci. **72**, 635 (1978).

[29] J. H. Onuferko and D. P. Woodruff, Surf. Sci. **95**, 555 (1980).

[30] W. S. Yang, F. Jona, and P. M. Marcus, Phys. Rev. B **27**, 1394 (1983).

[31] A. Scheidt, H. Richter, and U. Gerhardt, Surf. Sci. **205**, 38 (1988).

[32] F. Jensen, F. Besenbacher, E. Lægsgaard, and I. Stensgaard, Phys. Rev. B **42**, 9206 (1990).

[33] Ch. Wöll, R. J. Wilson, S. Chiang, H. C. Zeng, and K. A. R. Mitchell, Phys. Rev. B **42**, 11 926 (1990).

[34] T. Lederer, D. Arvanitis, G. Comelli, L. Tröger, and K. Baberschke, Phys. Rev. B **48**, 15 390 (1993).

[35] G. G. Tibbetts, J. M. Burkstrand, and J. C. Tracy, Phys. Rev. B **15**, 3652 (1977).

[36] D. T. Ling, J. N. Miller, D. L. Weissman, P. Pianetta, P. M. Stefan, I. Lindau, and W. E. Spicer, Surf. Sci. **95**, 89 (1980).

[37] A. Spitzer and H. Lüth, Surf. Sci. **118**, 121 (1982).

[38] R. A. DiDio, D. M. Zehner, and E. W. Plummer, J. Vac. Sci. Technol. A **62**, 852 (1984).

[39] P. V. Madhavan and M. D. Newton, J. Chem. Phys. **86**, 4030 (1986).

[40] A. Mattsson, I. Panas, P. Siegbahn, U. Wahlgren, and H. Åkeby, Phys. Rev. B **36**, 7389 (1987).

[41] P. Bagus and F. Illas, Phys. Rev. B **42**, 10 852 (1990).

[42] F. Illas, J. Rubio, and J. M. Ricart, J. Chem. Phys. **95**, 4225 (1991).

[43] A. Clotet, J. M. Ricart, J. Rubio, and F. Illas, Chem. Phys. **177**, 61 (1993).

[44] J. M. Ricart, J. Torras, F. Illas, and J. Rubio, Surf. Sci. **307-309**, 107 (1994).

[45] F. Besenbacher and J. K. Nørskov, Prog. Surf. Sci. **44**, 5 (1993).

[46] J. Nordgren and N. Wassdahl, Phys. Scr. **T31**, 103 (1990).

[47] Q. Dai and A. J. Gellman, Surf. Sci. **248**, 86 (1991).

[48] M. H. Mohamed and L. L. Kesmodel, Surf. Sci. **185**, L467 (1987).

[49] F. M. Leibsle, C. F. J. Flipse, and A. W. Robinson, Phys. Rev. B **47**, 15 865 (1993).

[50] M. Methfessel, D. Hennig, and M. Scheffler, Phys. Rev. B **46**, 4816 (1992).

[51] T. Kendelewicz, J. E. Klepeis, J. C. Woicik, S. H. Southworth, C. Mailhiot, M. van Schilfgaarde, M. Methfessel, A. Herrera-Gomez, and K. E. Miyano, Phys. Rev. B **51**, 10 774 (1995).

[52] D. M. Ceperley and B. J. Alder, Phys. Rev. Lett. **45**, 566 (1980).

[53] S. H. Vosko, L. Wilk, and M. Nusair, Can. J. Phys. **58**, 1200 (1980).

[54] P. E. Blöchl, O. Jepsen, and O. K. Andersen, Phys. Rev. B **49**, 16 223 (1994).

[55] J. E. Klepeis, L. J. Terminello, and D. A. Lapiano-Smith, Phys. Rev. B **53**, 16 035 (1996).

[56] R. S. Mulliken, J. Chem. Phys. **23**, 1833 (1955).

[57] R. Hoffmann, Rev. Mod. Phys. **60**, 601 (1988).

[58] H. Tillborg, A. Nilsson, B. Hernnäs, and N. Mårtensson, Surf. Sci. **269**, 300 (1992).

[59] T. Wiell, J. E. Klepeis, N. Wassdahl, A. Nilsson, P. Bennich, O. Björneholm, M. Samant, and J. Stöhr (to be published).

[60] L. O. Triguero and L. G. M. Pettersson, Surf. Sci. **398**, 70 (1998).